Acoustic-gravity waves interacting with the shelf break

Usama Kadri[1] and Michael Stiassnie[1]

Received 9 October 2011; revised 16 January 2012; accepted 2 February 2012; published 22 March 2012.

[1] A mathematical solution of the two-dimensional linear problem of an acoustic-gravity wave propagating over a bottom with a step, in a slightly compressible ocean, is presented. Expressions for the flow field on both sides of the step are derived. Furthermore, an extended problem is given that provides a solution for a group of acoustic-gravity waves, generated by a submarine earthquake, propagating toward a continental shelf. The dynamic bottom pressure produced by the acoustic-gravity waves is probably measurable, especially at the vicinity of the seaward face of the shelf break where incident and reflected modes appear simultaneously. A successful recording of such bottom pressures could assist in the early detection of tsunami.

Citation: Kadri, U., and M. Stiassnie (2012), Acoustic-gravity waves interacting with the shelf break, *J. Geophys. Res.*, *117*, C03035, doi:10.1029/2011JC007674.

1. Introduction

[2] The aim of the current work is to study the behavior of *acoustic-gravity* waves approaching a continental shelf. Acoustic-gravity waves may form in ocean from various sources, e.g., submarine earthquakes, landslides, fall of meteors, or underwater explosions. The mathematical formulation of the problem requires accounting for the slight compressibility of the ocean in order to obtain propagating wave modes other than the gravity mode (i.e., acoustic-gravity modes).

[3] The fluid mechanics significance of the slight compressibility of the ocean has been investigated by a number of researchers. *Miyoshi* [1954], *Sells* [1965], *Kajiura* [1970], *Yamamoto* [1982], *Nosov* [1999], *Nosov and Kolesov* [2007], *Chierici et al.* [2010], and *Stiassnie* [2010] have all investigated aspects of tsunami generation in a compressible ocean.

[4] *Yamamoto* [1982] provides an analytical solution of the problem of gravity and acoustic-gravity waves generated by vertical oscillation of a block of ocean floor. Further investigation of the acoustic-gravity waves has been carried out by *Stiassnie* [2010], who addressed the problem of a sudden rise of a block of the ocean floor. As the block rises, acoustic-gravity waves propagating at various frequencies are released. *Stiassnie* [2010] provides an analytical tool to calculate the leading acoustic-gravity wave modes.

[5] In this paper we formulate and solve the two-dimensional mathematical problem of an acoustic-gravity wave mode, referred to as an *incident* wave mode, propagating over a bottom with a step in a compressible fluid. We then extend the problem and solve for an incident group of acoustic-gravity wave modes generated by a submarine earthquake. As the modes approach a shelf break part of the energy is reflected whereas the other part is transmitted. The general solution of the problem enables us to obtain an expression for the dynamic bottom pressure.

[6] The formulation of the mathematical problem is introduced in section 2. The solution of a single incident wave is presented in section 3. A detailed example of acoustic-gravity waves, from a submarine earthquake, propagating toward a continental shelf, and the results, are presented in sections 4 and 5. Finally, concluding remarks are given in section 6.

2. Formulation and Basics

2.1. Formulation

[7] Consider the two-dimensional problem of a wave mode propagating over a bottom with a step in an ideal compressible fluid, with constant frequency ω, as presented in Figure 1 ($h_1 > h_2$). As the wave mode reaches the step, part of the energy is reflected, whereas the other part is transmitted. The objective is to find the surface wave elevation $z = \eta(x, t)$, as well as the dynamic bottom pressure p_b. To this end, it is necessary to solve for the flow velocity potential $\phi(x, z, t)$. The governing equation is the two-dimensional wave equation

$$\frac{\partial^2\phi}{\partial t^2} = C_s^2\left[\frac{\partial^2\phi}{\partial x^2} + \frac{\partial^2\phi}{\partial z^2}\right], \qquad \text{on } -h \le z \le 0, \tag{1}$$

where C_s is the speed of sound, $h = h_1$ for $x < 0$ and $h = h_2$ for $x > 0$. The bottom and the combined free surface boundary conditions are

$$\frac{\partial\phi}{\partial z} = 0, \qquad \text{on } z = -h, \tag{2}$$

and

$$\frac{\partial^2\phi}{\partial t^2} + g\frac{\partial\phi}{\partial z} = 0, \qquad \text{on } z = 0, \tag{3}$$

[1]Faculty of Civil and Environmental Engineering, Technion Israel Institute of Technology, Haifa, Israel.

0148-0227/12/2011JC007674

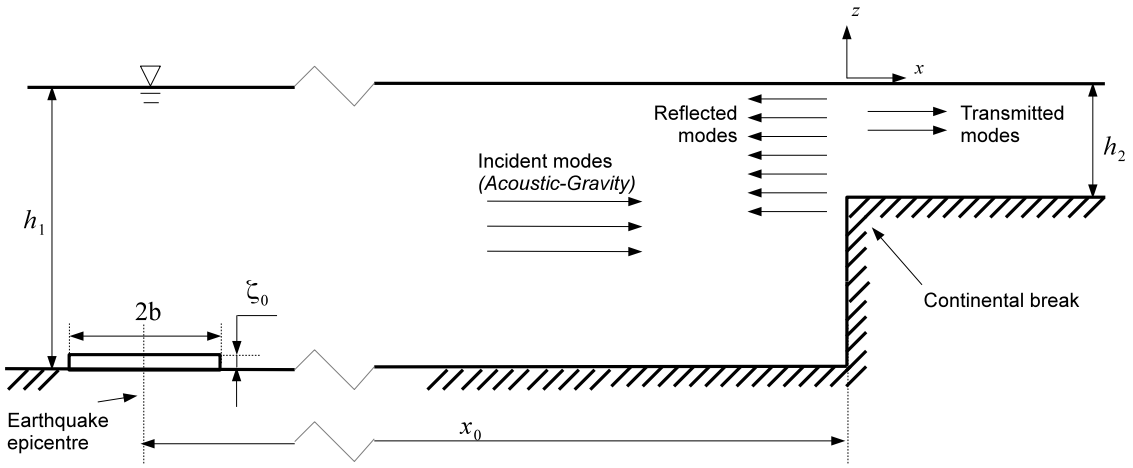

Figure 1. Schematic representation of the flow domain; h_1 and h_2 are depths of the ocean and continental shelf, respectively; $2b$ and ζ_0 are lateral and vertical extents of the bottom motion; x_0 is distance between earthquake epicenter and shelf break.

respectively, where g is the acceleration due to gravity. The lateral boundary conditions include the Sommerfield radiation condition at $|x| \to \infty$, and

$$\frac{\partial \phi}{\partial x} = 0, \qquad \text{on } z = 0 \quad \text{and} - h_1 < z < -h_2. \tag{4}$$

[8] The free surface elevation and the bottom pressure are then given by

$$\eta(x,t) = \frac{1}{g}\frac{\partial \phi}{\partial t}, \qquad \text{on } z = 0, \tag{5}$$

and

$$p_b(x,t) = \rho_s \frac{\partial \phi}{\partial t}, \qquad \text{on } z = -h, \tag{6}$$

where ρ_s is the density of water at the free surface.

2.2. Basics

[9] In a domain with constant depth, one can use the method of separation of variables to obtain basic solutions all with a prescribed frequency ω:

$$\phi_n = \alpha_n f_n(z) e^{i(k_n x - \omega t)}, \qquad n = 0, 1, 2, \ldots \tag{7}$$

for any amplitude α_n.

[10] A Sturm-Liouville problem in $z \in (-h, 0)$ yields the orthonormal eigenfunctions

$$f_n(z) = \frac{\cosh[\kappa_n(h+z)]}{\sqrt{I_n}}, \tag{8a}$$

where

$$I_n^{(j)} = \int_{-h}^{0} \cosh^2[\kappa_n(h+z)]dz, \tag{8b}$$

as well as the eigenvalues κ_n, which are solutions of the dispersion equation

$$\omega^2 = g\kappa_n \tanh(\kappa_n h). \tag{9}$$

The wave numbers k_n, in equation (7), are given by

$$k_n^2 = \kappa_n^2 + \frac{\omega^2}{C_s^2}. \tag{10}$$

[11] The first eigenvalue κ_0 is real, whereas all the rest are pure imaginary. The first wave number k_0, which corresponds to a gravity wave, is always real. The following $N_{a.g.}$ wave numbers, $[k_1, k_2, .., k_{N_{a.g.}}]$, where $N_{a.g.}$ is the nearest integer smaller than $[\omega h/\pi C_s + 1/2]$, are also real and are called acoustic-gravity (or hydroacoustic) waves. The gravity and the acoustic-gravity modes are all progressive waves. The wave numbers $[k_{N_{a.g.}+1}, k_{N_{a.g.}+2}, \ldots]$ are all imaginary and correspond to decaying evanescent modes.

[12] Following *Yamamoto* [1982], one can show that the average energy flux of the progressive modes is given by

$$\overline{F}_n = \frac{1}{2}\rho_s \omega k_n |\alpha_n|^2, \qquad n = 0, 1, .., N_{a.g.} \tag{11}$$

3. Solution for a Single Incident Wave

[13] The solution at the deep seaward face of the break (left side), denoted by (1), is given by the incident wave mode, denoted by $\hat{i}$ (with $\alpha_{\hat{i}} = 1$), and an infinite sum of all modes which either propagate to the left or decay for $x \to -\infty$:

$$\Phi^{(1)} = \frac{\cosh[\kappa_{\hat{i}}^{(1)}(h_1+z)]}{\sqrt{I_{\hat{i}}^{(1)}}} e^{i(k_{\hat{i}}^{(1)}x - \omega t)} + \sum_{n=0}^{\infty} \left(\alpha_n^{(1)} \frac{\cosh[\kappa_n^{(1)}(h_1+z)]}{\sqrt{I_n^{(1)}}} e^{-i(k_n^{(1)}x + \omega t)} \right). \tag{12}$$

The solution in the shallow shoreward face of the break (right side), denoted by (2), is given as an infinite sum of all modes which either propagate to the right or decay for $x \to \infty$:

$$\Phi^{(2)} = \sum_{n=0}^{\infty} \left(\alpha_n^{(2)} \frac{\cosh[\kappa_n^{(2)}(h_2+z)]}{\sqrt{I_n^{(2)}}} e^{i(k_n^{(2)}x-\omega t)} \right). \tag{13}$$

From equation (5), the corresponding surface wave elevations are

$$\eta^{(1)} = -\frac{i\omega}{g} \frac{\cosh\left(\kappa_{\hat{i}}^{(1)} h_1\right)}{\sqrt{I_{\hat{i}}^{(1)}}} e^{i(k_{\hat{i}}^{(1)}x-\omega t)}$$

$$-\frac{i\omega}{g} \sum_{n=0}^{\infty} \left(\alpha_n^{(1)} \frac{\cosh\left(\kappa_n^{(1)} h_1\right)}{\sqrt{I_n^{(1)}}} e^{-i(k_n^{(1)}x+\omega t)} \right), \tag{14}$$

and

$$\eta^{(2)} = -\frac{i\omega}{g} \sum_{n=0}^{\infty} \left(\alpha_n^{(2)} \frac{\cosh\left(\kappa_n^{(2)} h_2\right)}{\sqrt{I_n^{(2)}}} e^{i(k_n^{(2)}x-\omega t)} \right). \tag{15}$$

The corresponding free surface amplitudes are given by

$$a_n^{(j)} = \frac{\omega}{g} |\alpha_n^{(j)}| \frac{\cosh\left(\kappa_n^{(j)} h_j\right)}{\sqrt{I_n^{(j)}}}. \tag{16}$$

[14] The amplitudes of the potential $\alpha_n^{(j)}$ (j = 1, 2) are unknowns, which are found from the following matching conditions (given by *O'Hare and Davies* [1992] for gravity waves)

$$\Phi^{(1)} = \Phi^{(2)}, \quad \text{for } x = 0, \quad \text{and} - h_2 < z < 0, \tag{17}$$

$$\frac{\partial \Phi^{(1)}}{\partial x} = \begin{cases} 0, & \text{for} \quad x = 0, \quad -h_1 < z < -h_2 \\ \partial \Phi^{(2)}/\partial x, & \text{for} \quad x = 0, \quad -h_2 < z < 0. \end{cases} \tag{18}$$

[15] Substituting equations (12) and (13) into equations (17) and (18) and using the orthonormal identity of the eigenfunctions $f_n^{(1)}(z)$ in $z \in (-h_1, 0)$ and $f_n^{(2)}(z)$ in $z \in (-h_2, 0)$ (see equations (8a) and (8b)) yields

$$J_{\hat{i},M} + \sum_{n=0}^{\infty} \left(\alpha_n^{(1)} J_{n,M} \right) = \alpha_M^{(2)}, \qquad M = 0, 1, 2, \ldots \tag{19}$$

and

$$ik_{\hat{i}}^{(1)} \delta_{\hat{i}M} - ik_M^{(1)} \alpha_M^{(1)} = \sum_{m=0}^{\infty} \left(ik_m^{(2)} \alpha_m^{(2)} J_{M,m} \right), M = 0, 1, 2, \ldots \tag{20}$$

where $\delta_{\hat{i},M}$ is the Kronecker delta, and

$$J_{n,m} = \int_{-h_j}^{0} \frac{\cosh[\kappa_n^{(1)}(h_1+z)] \cosh[\kappa_m^{(2)}(h_2+z)]}{\sqrt{I_n^{(1)} I_m^{(2)}}} \mathrm{d}z. \tag{21}$$

Dividing equation (20) by i and substituting $\alpha_m^{(2)}$ from equation (19) into equation (20) gives

$$\sum_{n=0}^{\infty} \left(\sum_{m=0}^{\infty} \left(k_n^{(2)} J_{M,n} J_{m,n} \alpha_m^{(1)} \right) \right) + k_M^{(1)} \alpha_M^{(1)}$$

$$= k_{\hat{i}}^{(1)} \delta_{\hat{i},M} - \sum_{n=0}^{\infty} \left(k_n^{(2)} J_{M,n} J_{\hat{i},n} \right), \qquad M = 0, 1, 2, \ldots \tag{22}$$

Equation (22) is a system of infinite linear algebraic equations with infinite unknowns $\alpha_m^{(1)}$. This system of equations can be written in a matrix form and truncated to $M + 1$ equations with $M + 1$ unknowns as follows:

$$\underbrace{\begin{pmatrix} G_{0,0}+k_0^{(1)} & G_{0,1} & \ldots & G_{0,M} \\ G_{1,0} & G_{1,1}+k_1^{(1)} & \ldots & G_{1,M} \\ \vdots & \vdots & \ddots & \vdots \\ G_{\hat{i},0} & \ddots & G_{\hat{i},\hat{i}}+k_{\hat{i}}^{(1)} & \vdots \\ \vdots & \vdots & \ddots & \vdots \\ G_{M,0} & G_{M,1} & \ldots & G_{M,M} \end{pmatrix}}_{\boldsymbol{A}}$$

$$\cdot \underbrace{\begin{pmatrix} \alpha_0^{(1)} \\ \alpha_1^{(1)} \\ \vdots \\ \alpha_{\hat{i}}^{(1)} \\ \vdots \\ \alpha_M^{(1)} \end{pmatrix}}_{\boldsymbol{\alpha}^{(1)}} = \underbrace{\begin{pmatrix} F_0 \\ F_1 \\ \vdots \\ k_{\hat{i}}^{(1)} + F_{\hat{i}} \\ \vdots \\ F_M \end{pmatrix}}_{\boldsymbol{B}} \tag{23}$$

where

$$G_{\mu,m} = \sum_{n=0}^{M} \left(k_n^{(2)} J_{\mu,n} J_{m,n} \right), \qquad \mu = 0, 1, \ldots, M \tag{24}$$

and

$$F_{\mu} = \sum_{n=0}^{M} \left(k_n^{(2)} J_{\mu,n} J_{\hat{i},n} \right), \qquad \mu = 0, 1, \ldots, M. \tag{25}$$

Once the matrix $\boldsymbol{A}$ and the vector $\boldsymbol{B}$ are calculated, the amplitude of the velocity potential on the left side of the step, $\boldsymbol{\alpha}^{(1)}$, is found from equation (23):

$$\boldsymbol{\alpha}^{(1)} = \boldsymbol{A}^{-1} \boldsymbol{B}. \tag{26}$$

Once $\boldsymbol{\alpha}^{(1)}$ is found, the unknown amplitude vector $\boldsymbol{\alpha}^{(2)}$ (related to the right side of the step) is obtained from equation (19).

4. Acoustic-Gravity Waves From a Submarine Earthquake Propagating Toward a Continental Shelf: A Numerical Example

[16] In section 3 we introduced a solution for a single incident acoustic-gravity mode interacting with a step. Now, we consider a group of N incident acoustic-gravity modes,

generated by a submarine earthquake, propagating toward a continental shelf as shown in Figure 1. In the current example, the depths of the ocean and the continental shelf are $h_1 = 4000$ m, and $h_2 = 250$ m, respectively. The distance between the earthquake epicenter and the shelf break is $x_0 = 10^6$ m. The speed of sound of water is $C_s = 1500$ m/s, and the acceleration due to gravity is taken as $g = 10$ m/s^2. Following *Nosov* [1999], the motion of the bottom is given by

$$\frac{\partial \zeta(x,t)}{\partial t} = \frac{\zeta_0}{\tau}\mathcal{H}\left(b^2 - (x+x_0)^2\right)\mathcal{H}[t(\tau - t)], \tag{27}$$

where $\zeta_0 = 1$ m, $b = 4 \times 10^4$ m, and $\tau = 10$ s, are the vertical and the lateral extents, and the duration of the bottom motion, respectively. The function $\mathcal{H}$ is the Heaviside function. Note that apart from the bottom motion due to the earthquake, the bottom is assumed rigid. Following *Stiassnie* [2010], the incident acoustic-gravity modes at $(0, t_0)$ propagate each at a specific frequency given by

$$\omega_i = \frac{\acute{\kappa}_i^{(1)} C_s}{\sqrt{1 - (x_0/C_s t_0)^2}}, \tag{28}$$

where $\acute{\kappa}_i^{(1)}$ is real ($\kappa_i^{(1)} = i\acute{\kappa}_i^{(1)}$), and the corresponding wave numbers $k_i^{(1)}$ are

$$k_i^{(1)} = \frac{\acute{\kappa}_i^{(1)} x_0/C_s t_0}{\sqrt{1 - (x_0/C_s t_0)^2}}. \tag{29}$$

Note that $\hat{\imath}$ indicates the sequence order of $\acute{\kappa}_i^{(1)}$ given by

$$\acute{\kappa}_i h \approx \left(\hat{\imath} - \frac{1}{2}\right)\pi, \qquad \text{for } \hat{\imath} = 1, 2, \ldots. \tag{30}$$

Considering a sum of N incident modes, each with its own frequency ω_i and the corresponding wave number $k_i^{(1)}$, given by equations (28) and (29), so that

$$\Phi^{(j)} = \sum_{\hat{\imath}=1}^{N} \beta_{\hat{\imath}}^{(1)} \Phi_{\hat{\imath}}^{(j)}(\omega_i), \tag{31}$$

where $\Phi_{\hat{\imath}}^{(j)}(\omega)$ is the velocity potential on the jth side of the break caused by the $\hat{\imath}$th incident mode. Each $\Phi_{\hat{\imath}}^{(j)}(\omega)$ $(\hat{\imath} = 1, 2, \ldots, N)$ is solved separately based on the solution given in section 3. The potential $\Phi^{(j)}$ is the total velocity potential on the jth side of the break, caused by all N incident modes. The $\beta_{\hat{\imath}}^{(1)}$ are the complex amplitudes of the incident modes that are evaluated from the surface elevation at $(0, t_0)$.

[17] The nondimensional surface elevation is given in equation (4.1) of *Stiassnie* [2010], who applied the method of stationary phase to the propagating acoustic-gravity wave modes. The dimensional form of this equation is given by

$$\eta^{(1)}(\tilde{x},\tilde{t}) = -\zeta_0 \sum_{\hat{\imath}=1}^{N} \frac{2^{5/2}\tilde{t}^{1/2}\left(1 - (\tilde{x}/C_s\tilde{t})^2\right)^{5/4}}{\sqrt{\pi}\left(\acute{\kappa}_{\hat{\imath}}^{(1)}\right)^{5/2} {C_s}^{1/2}\tau\tilde{x}h_1}$$

$$\cdot \sin\left(\frac{\acute{\kappa}_{\hat{\imath}}^{(1)} C_s\tau/2}{\sqrt{1 - (\tilde{x}/C_s\tilde{t})^2}}\right)\sin\left(\frac{\acute{\kappa}_{\hat{\imath}}^{(1)} b\tilde{x}/(C_s\tilde{t})}{\sqrt{1 - (\tilde{x}/C_s\tilde{t})^2}}\right)$$

$$\cdot \exp\left(-i\left(\acute{\kappa}_{\hat{\imath}}^{(1)}\sqrt{{C_s}^2\tilde{t}^2 - \tilde{x}^2} + \frac{\pi}{4}\right)\right). \tag{32}$$

Substituting $\tilde{x} = x_0 + x$ and $\tilde{t} = t_0 + t$ into equation (32) gives

$$\eta^{(1)} = -\zeta_0 \sum_{\hat{\imath}=1}^{N} \frac{2^{5/2} {t_0}^{1/2}\left(1 - (x_0/C_s t_0)^2\right)^{5/4}}{\sqrt{\pi}\left(\acute{\kappa}_{\hat{\imath}}^{(1)}\right)^{5/2} {C_s}^{1/2}\tau x_0 h_1}$$

$$\cdot \sin\left(\frac{\acute{\kappa}_{\hat{\imath}}^{(1)} C_s\tau/2}{\sqrt{1 - (x_0/C_s t_0)^2}}\right)\sin\left(\frac{\acute{\kappa}_{\hat{\imath}}^{(1)} bx_0/(C_s t_0)}{\sqrt{1 - (\tilde{x}/C_s t_0)^2}}\right)$$

$$\cdot \exp\left(-i\left(\acute{\kappa}_{\hat{\imath}}^{(1)}\sqrt{{C_s}^2 {t_0}^2 - {x_0}^2} + \frac{\pi}{4} + \omega_i t - k_{\hat{\imath}}^{(1)} x\right)\right). \tag{33}$$

[18] Comparing equation (33) to the incident mode term on the right-hand side of equation (14), we obtain an expression for $\beta_{\hat{\imath}}^{(1)}$:

$$\beta_{\hat{\imath}}^{(1)} = -i\frac{g}{\omega_{\hat{\imath}}}\frac{\zeta_0\sqrt{I_{\hat{\imath}}^{(1)}}}{\cos\left(\acute{\kappa}_{\hat{\imath}}^{(1)}\right)}\frac{2^{5/2} {t_0}^{1/2}\left(1 - (x_0/C_s t_0)^2\right)^{5/4}}{\sqrt{\pi}\left(\acute{\kappa}_{\hat{\imath}}^{(1)}\right)^{5/2} {C_s}^{1/2}\tau x_0 h_1}$$

$$\cdot \sin\left(\frac{\acute{\kappa}_{\hat{\imath}}^{(1)} C_s\tau/2}{\sqrt{1 - (x_0/C_s t_0)^2}}\right)\sin\left(\frac{\acute{\kappa}_{\hat{\imath}}^{(1)} bx_0/(C_s t_0)}{\sqrt{1 - (\tilde{x}/C_s t_0)^2}}\right)$$

$$\cdot \exp\left(-i\left(\acute{\kappa}_{\hat{\imath}}^{(1)}\sqrt{{C_s}^2 {t_0}^2 - {x_0}^2} + \frac{\pi}{4}\right)\right). \tag{34}$$

Figure 2 presents the temporal evolution of the free surface of the $\hat{\imath} = 1, 2, \ldots, 25$ ($N = 25$) leading acoustic-gravity wave modes arriving at the shelf break. The calculations' domain, $t \in$ (2665 s, 2745 s), denoted on Figure 2, was chosen due to the homogeneousness of the oscillations of the first acoustic-gravity wave mode (leading mode). At the chosen time domain, with $t_0 = 2705$ s, acoustic-gravity waves arrive 40 min prior to the arrival of the tsunami. It is worth noting that the tsunami, propagating at a velocity of $\sqrt{gh_1}$, arrives at the shelf break at $t = 5000$ s (83 min from the epicenter to the

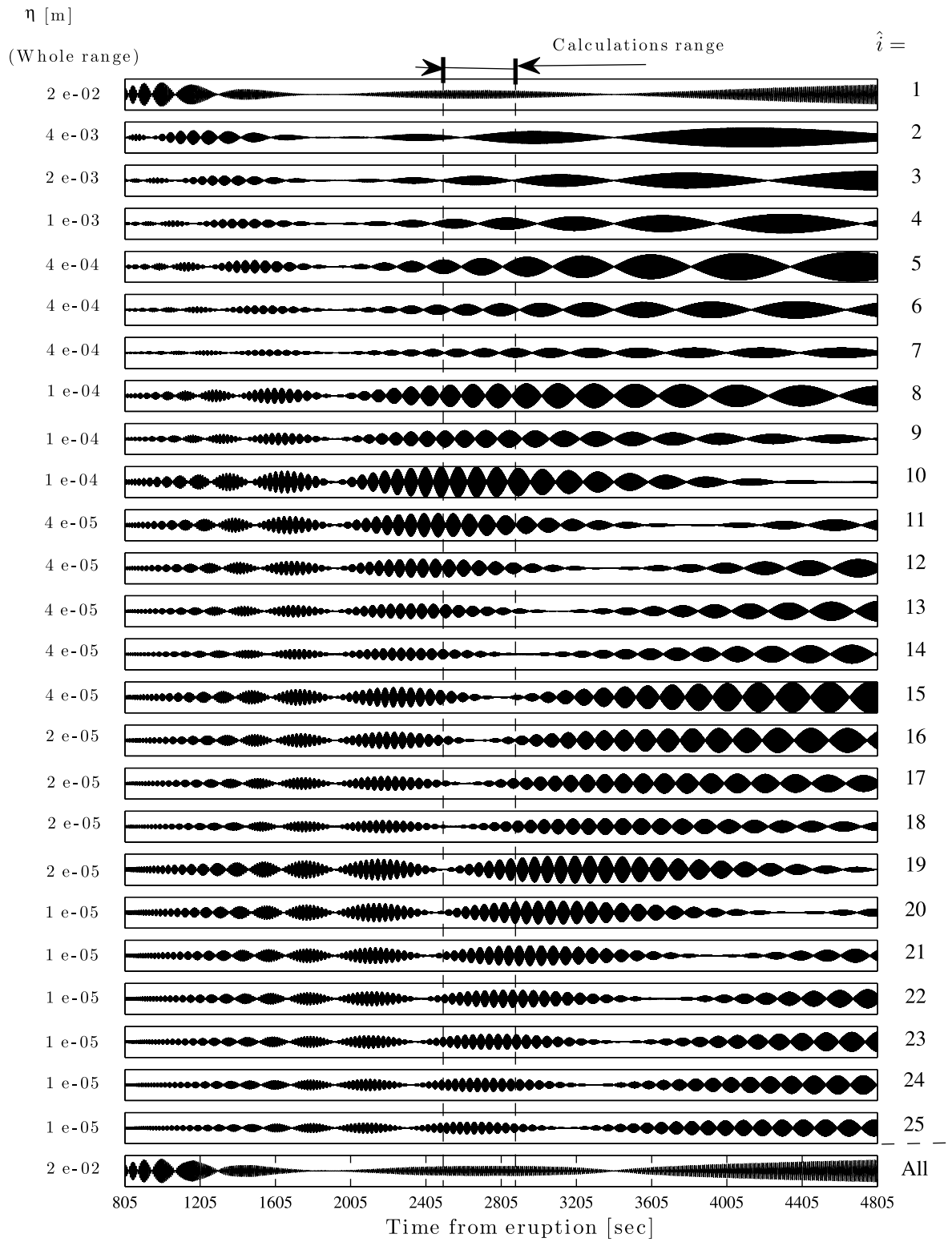

Figure 2. Temporal evolution of the free surface of the first 25 leading acoustic-gravity wave modes arriving at the continental shelf.

break), whereas the first acoustic-gravity waves reach the break at $t = 800$ s (70 min prior to the arrival of the tsunami).

[19] Note that the vertical axes in Figure 2 are all symmetric, and due to space limitations the labels are for the whole range of each axis. From Figure 2 we conclude that the height of the wave decreases with the mode number, and the first acoustic-gravity mode is the dominant mode, in that context. This could also be observed by comparing the first mode case with the superposition of all 25 modes given at the bottom of Figure 2.

Table 1. Summary of Inputs

Parameter	Value
Gravitational constant	$g = 10$ m/s^2
Water density	$\rho_s = 1000$ kg/m^3
Speed of sound	$C_s = 1500$ m/s
Ocean depth	$h_1 = 4000$ m
Shelf depth	$h_2 = 250$ m
Vertical extent of bottom motion	$\zeta_0 = 1$ m
Lateral extent of bottom motion	$b = 4 \times 10^4$ m
Duration of bottom motion	$\tau = 10$ (s)
Distance between the earthquake and shelf break	$x_0 = 10^6$ m
Time domain of observation	$t = 2500 \ldots 2900$ s
Number of incident acoustic-gravity modes	$N = 25$
Total number of acoustic-gravity and evanescent modes	$M = 30$

[20] The total dynamic bottom pressure caused by all N incident modes is

$$p_b^{(j)} = \sum_{\hat{\imath}=1}^{N} \beta_{\hat{\imath}}^{(1)} p_{b,\hat{\imath}}^{(j)}(\omega_{\hat{\imath}}), \tag{35}$$

where $p_{b,\hat{\imath}}^{(j)}(\omega_{\hat{\imath}})$ is the dynamic bottom pressure caused by the $\hat{\imath}$th incident mode calculated by equation (6).

[21] Since the energy flux of each incident mode is either reflected or transmitted, the calculation error, $\mathrm{err}_{\hat{\imath}}$ (of each incident mode), could be estimated by

$$\mathrm{err}_{\hat{\imath}} = 1 - \frac{\sum \overline{F}_{ref} + \sum \overline{F}_{tr}}{\overline{F}_{\hat{\imath}}}, \tag{36}$$

where $\overline{F}_{\hat{\imath}}$ is the energy flux of the incident mode and $\overline{F}_{ref}$ and $\overline{F}_{tr}$ are the corresponding energy fluxes reflected and transmitted, respectively.

[22] The initial amplitudes and the specific frequencies of each of the incident modes interacting with the shelf break are calculated for $t_0 = 2705$ s, as an example, using equations (34) and (28), respectively. Since the problem is linear, we solve for each incident mode separately and then superpose all solutions. In order to retain the same number of modes in the system of equations solved for each incident mode, we set the total number of modes to 31 ($M = 30$). In general, for the $\hat{\imath}$th incident mode ($\hat{\imath} = 1, \ldots, N$) there is a single gravity mode, $\hat{\imath}$ acoustic-gravity modes, and $(M - \hat{\imath})$ *evanescent* modes on the left side of the break. However, there is a single gravity mode, $N_{a.g.}$ acoustic-gravity modes, and $(M - N_{a.g.})$ evanescent modes on the right side of the break. The input of the problem is summarized in Table 1.

5. Results

[23] Table 2 presents the following values for each incident mode $\hat{\imath}$: frequency $\omega_{\hat{\imath}}$, wave number $k_{\hat{\imath}}$, incident wave amplitude $a_{\hat{\imath}}$, group velocity $C_{g,\hat{\imath}}$ ($\equiv \mathrm{d}\omega_{\hat{\imath}}/\mathrm{d}k_{\hat{\imath}}$), phase velocity $C_{p,\hat{\imath}}$, wavelength $\lambda_{\hat{\imath}}$, and the absolute error in the flux balance $\mathrm{err}_{\hat{\imath}}$. For each incident mode $\hat{\imath}$ there are $r = 1, \ldots, \hat{\imath}$ reflected modes all propagate at the same frequency $\omega_{\hat{\imath}}$. Only the $\hat{\imath}$th reflected mode has the same wave properties as the incident mode. The phase velocity and the wavelength decrease with r (for each incident mode $\hat{\imath}$). It is notable that the incident modes propagate all at similar group and phase velocities which implies that they propagate temporally and spatially as a group. It is also remarkable that the error in the normalized flux balance is enormously small ($O(10^{-17})$ to $O(10^{-12})$) for the first 8 incident modes, which are fully reflected. Thus, no acoustic-gravity modes exist on the right side of the break. However, starting from mode 9 the error is $O(10^{-4})$ to $O(10^{-2})$, probably due to the beginning of transmission to acoustic-gravity modes. The error decreases if the number of modes M is increased. The consequences of the appearance

Table 2. Values for the First 25 Incident Modes[a]

$\hat{\imath}$	$\omega_{\hat{\imath}}$ (rad/s)	$k_{\hat{\imath}}$ (rad/m)	$\lambda_{\hat{\imath}}$ (km)	$a_{\hat{\imath}}$ (m)	$C_{g,\hat{\imath}}$ (m/s)	$C_{p,\hat{\imath}}$ (m/s)	$\mathrm{err}_{\hat{\imath}}$
1	0.608	8.890×10^{-5}	70.7	5.877×10^{-3}	324.87	6837	7.57×10^{-12}
2	1.824	2.966×10^{-4}	21.2	3.062×10^{-3}	365.53	6147	3.52×10^{-14}
3	3.039	4.982×10^{-4}	12.6	1.919×10^{-3}	368.64	6101	9.87×10^{-15}
4	4.255	6.989×10^{-4}	8.99	1.158×10^{-3}	369.49	6088	1.52×10^{-15}
5	5.471	8.993×10^{-4}	6.99	6.237×10^{-4}	369.84	6083	1.77×10^{-15}
6	6.687	1.099×10^{-3}	5.71	2.758×10^{-4}	370.01	6080	1.17×10^{-15}
7	7.902	1.299×10^{-3}	4.83	8.399×10^{-5}	370.11	6079	5.06×10^{-17}
8	9.118	1.500×10^{-3}	4.19	8.409×10^{-6}	370.18	6078	3.27×10^{-17}
9	10.33	1.700×10^{-3}	3.70	3.744×10^{-6}	370.22	6077	1.22×10^{-3}
10	11.55	1.900×10^{-3}	3.31	2.810×10^{-5}	370.25	6077	6.61×10^{-3}
11	12.77	2.100×10^{-3}	2.99	5.129×10^{-5}	370.27	6076	1.51×10^{-2}
12	13.98	2.300×10^{-3}	2.73	5.850×10^{-5}	370.29	6076	2.52×10^{-2}
13	15.20	2.501×10^{-3}	2.51	4.885×10^{-5}	370.30	6076	3.53×10^{-2}
14	16.41	2.701×10^{-3}	2.33	3.007×10^{-5}	370.31	6076	4.35×10^{-2}
15	17.63	2.901×10^{-3}	2.17	1.204×10^{-5}	370.32	6076	4.83×10^{-2}
16	18.84	3.101×10^{-3}	2.03	1.646×10^{-6}	370.33	6076	4.89×10^{-2}
17	20.06	3.301×10^{-3}	1.90	4.934×10^{-7}	370.33	6076	4.52×10^{-2}
18	21.28	3.501×10^{-3}	1.79	5.612×10^{-6}	370.34	6076	3.80×10^{-2}
19	22.49	3.701×10^{-3}	1.70	1.199×10^{-5}	370.34	6076	2.86×10^{-2}
20	23.71	3.902×10^{-3}	1.61	1.541×10^{-5}	370.34	6075	1.88×10^{-2}
21	24.92	4.102×10^{-3}	1.53	1.426×10^{-5}	370.34	6075	1.01×10^{-2}
22	26.14	4.302×10^{-3}	1.46	9.645×10^{-6}	370.35	6075	3.71×10^{-3}
23	27.35	4.502×10^{-3}	1.40	4.259×10^{-6}	370.35	6075	3.31×10^{-4}
24	28.57	4.702×10^{-3}	1.34	6.817×10^{-7}	370.35	6075	5.32×10^{-4}
25	29.79	4.902×10^{-3}	1.28	1.043×10^{-7}	370.35	6075	1.75×10^{-3}

[a]Here $h_1 = 4000$ m, $h_2 = 250$ m, $g = 10$ m/s^2, $C_s = 1500$ m/s. Bold indicates an additional AG mode, thus at $\hat{\imath}$=>9 there is one additional AG mode, and at $\hat{\imath}$=>24 there is a second additional mode.

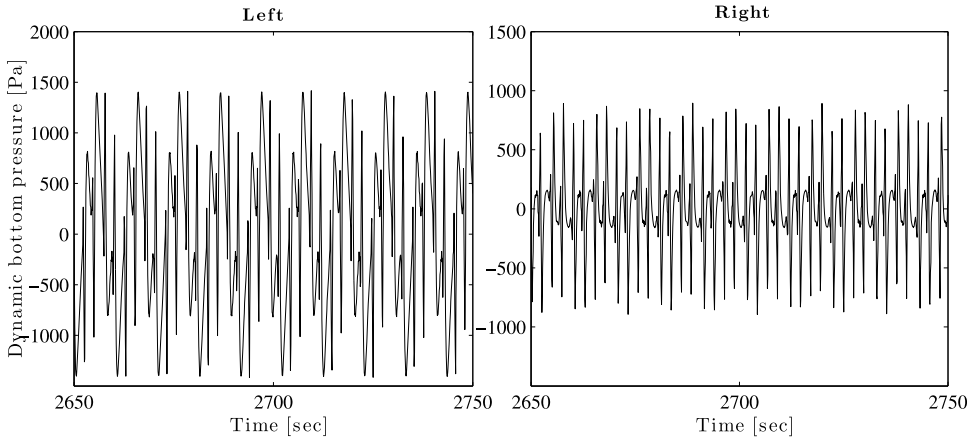

Figure 3. Calculations of the dynamic bottom pressure ($z = -h$), at the vicinity of the step ($x = 0$), both on the (left) left and (right) right sides of the shelf break.

of the high-frequency acoustic-gravity modes on the right side of the break are addressed in section 5.2.

5.1. Dynamic Bottom Pressure at the Vicinity of the Shelf Break, $x = 0$

[24] Figure 3 presents calculations of the total dynamic bottom pressure ($z = -h$) at the vicinity of the shelf break, both on left ($x = 0^-$) and right ($x = 0^+$). The number of incident modes is $N = 25$. The bottom pressure reaches a magnitude of about 1500 Pa (1.48×10^{-2} atm) and 1000 Pa (9.87×10^{-3} atm) on the left and right sides of the break, respectively. These magnitudes are probably sufficiently large for measurement purposes.

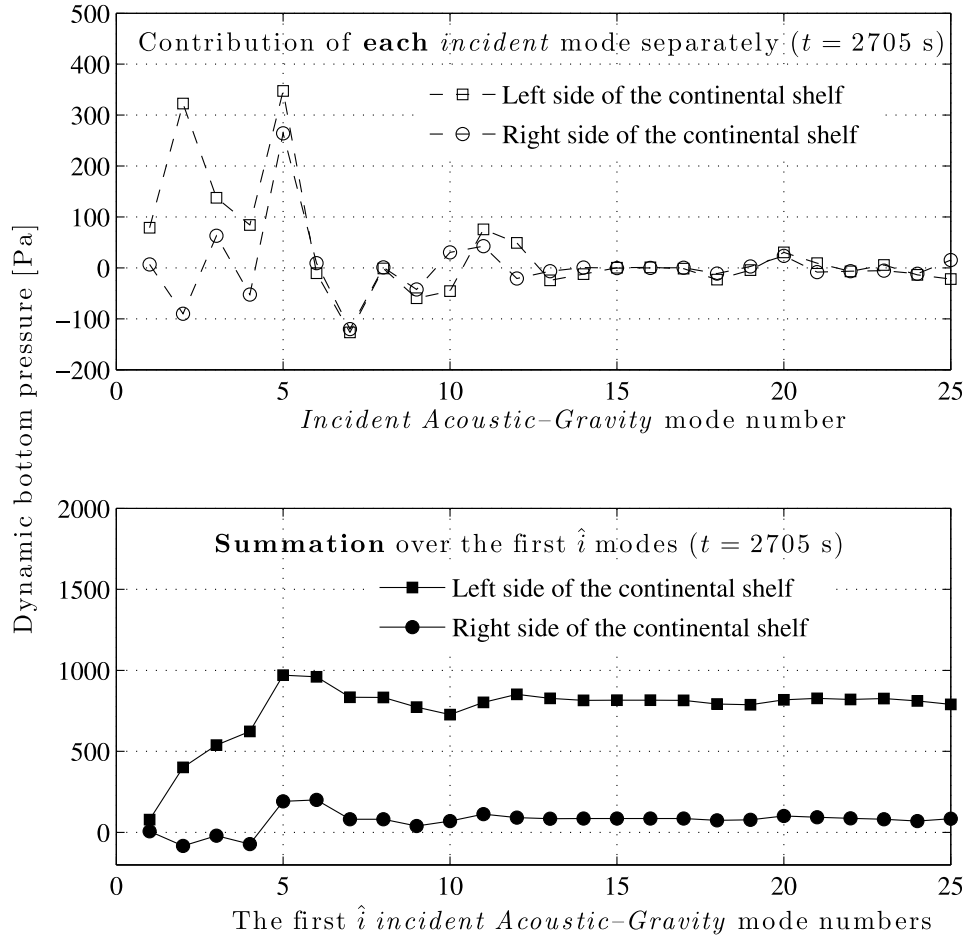

Figure 4. Dynamic bottom pressure (at $t = 2705$ s). (top) Contribution of each mode separately. (bottom) Summation over the first $\hat{\imath}$ modes.

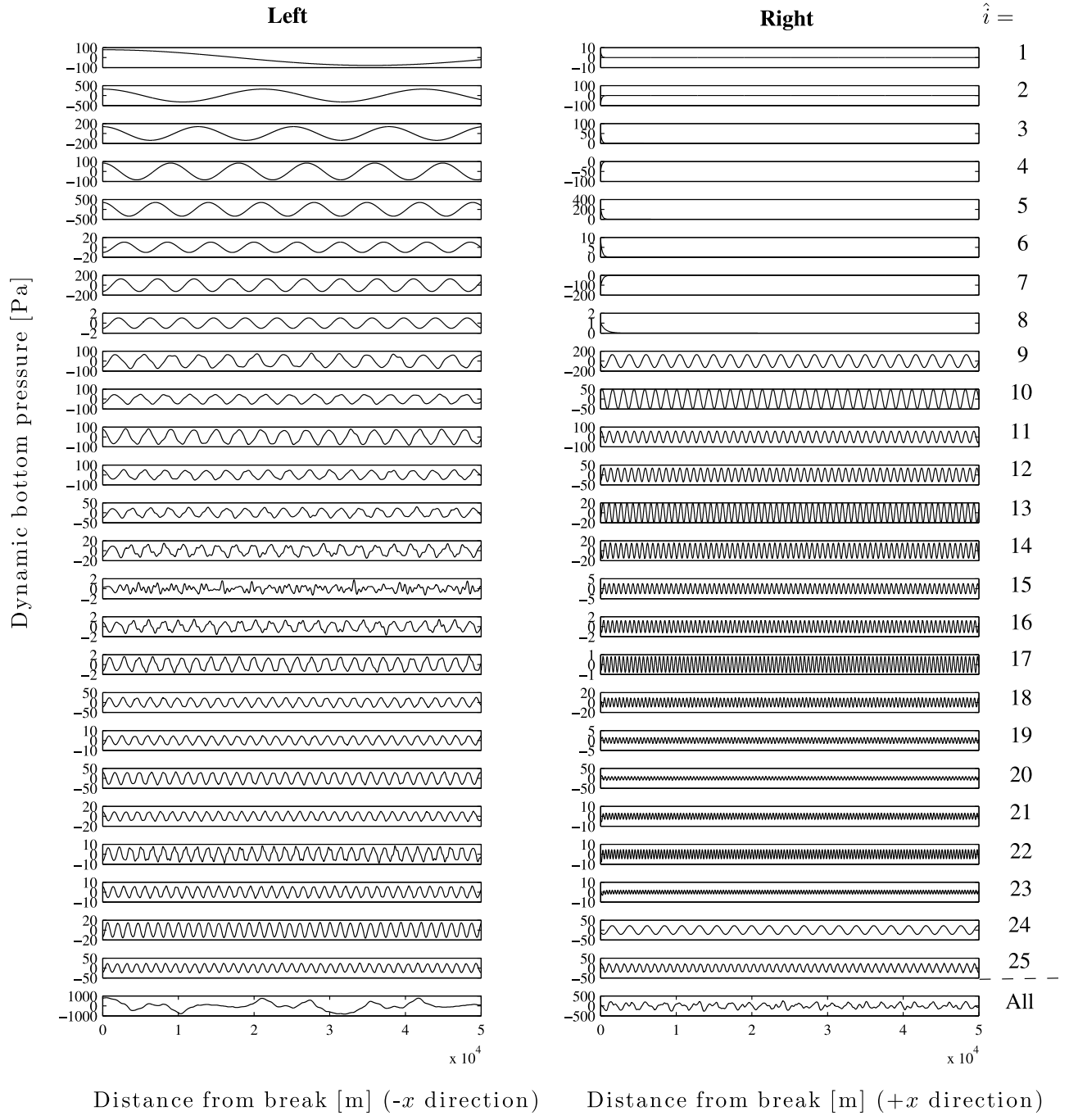

Figure 5. Contribution of modes to the dynamic bottom pressure (at t = 2705 s). (left) Left side of the shelf break. (right) Right side of the break.

[25] Different cases with additional evanescent modes have been tested from which we concluded that the dynamic bottom pressure is insensitive to additional evanescent modes. For example, the difference in the bottom pressure when considering 30 additional evanescent modes (M = 60) is as low as 0.14% and 2.22% for the left and right sides of the break, respectively. The latter (err = 2.22%) explains the increase in the error of the normalized flux for $\hat{\imath} \geq 9$, when M is limited to 30 (see Table 2).

[26] In order to decide on the number of the leading incident modes (acoustic-gravity) to be considered in the calculations we need to determine the convergence behavior of the dynamic bottom pressure as function of the number of incident modes considered. Figure 4 (top) presents the dynamic bottom pressure on both sides of the break as a consequence of a single incident mode $\hat{\imath} = 1, \ldots, N$ (dashed lines), whereas Figure 4 (bottom) presents the total pressure as a consequence of all incident modes $1, \ldots, \hat{\imath}$ (solid lines). The squares and circles represent the left and right sides of the shelf break, respectively. In both cases the total dynamic bottom pressure converges, and in this respect, calculating for the first seven incident modes is sufficient. However, a number of factors,

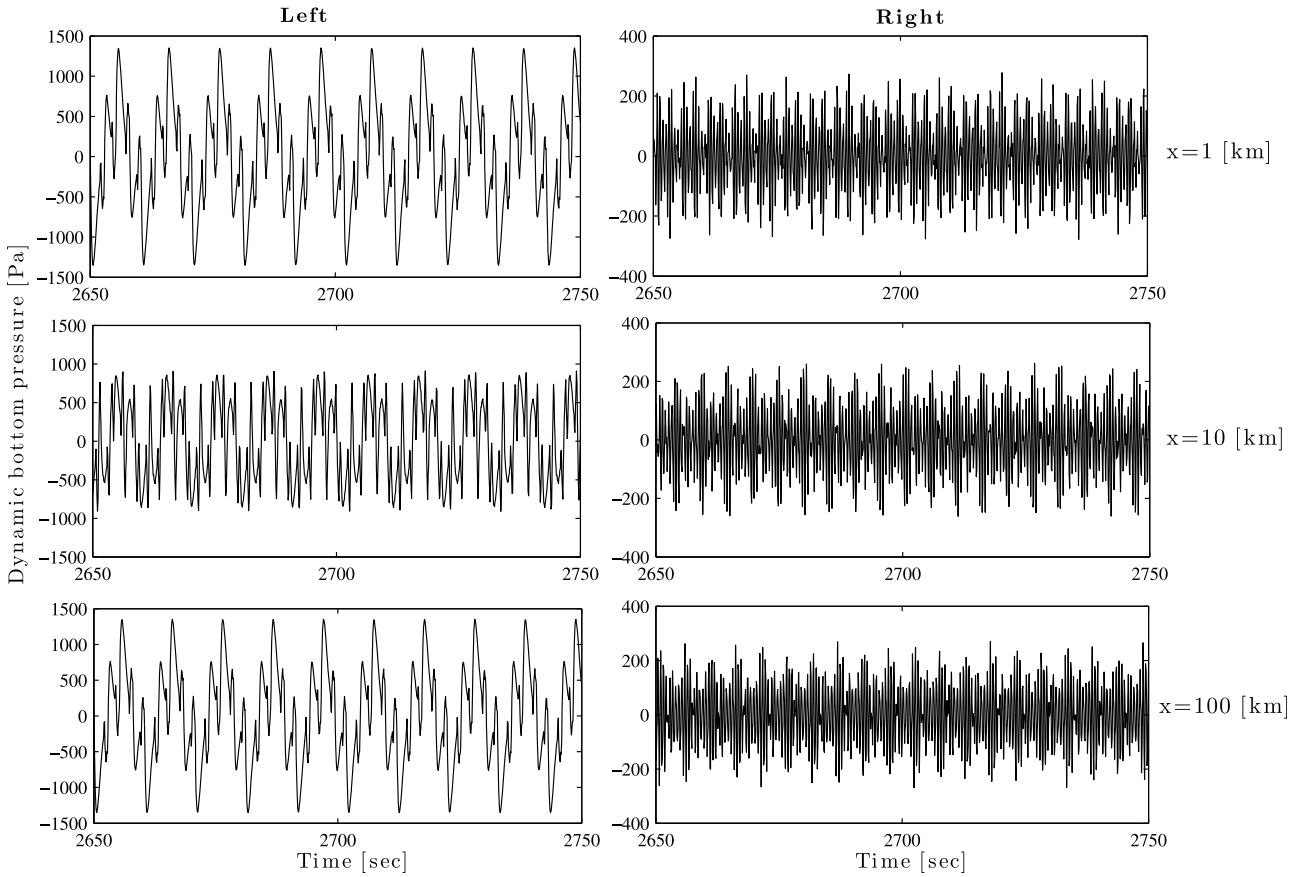

Figure 6. Temporal evolution of the dynamic bottom pressure at (top) $|x| = 1$ km, (middle) $|x| = 10$ km, and (bottom) $|x| = 100$ km. Superposed solution of all 25 incident modes.

other than convergence could demand a larger number of incident modes to be included, as further elaborated in section 5.2. Note that the wave amplitude decreases rather fast with the wave frequency, thus only the leading existing modes are of a significant importance.

5.2. Dynamic Bottom Pressure Away From the Shelf Break, $|x| > 0$

[27] As long as acoustic-gravity modes exist the dynamic bottom pressure will have an oscillatory nonvanishing spatial behavior. However, on the right side of the break, where the water is shallower, only acoustic-gravity modes with relatively high-frequency survive (e.g., $\hat{\imath} \geq 9$).

[28] Figure 5 presents calculations of the dynamic bottom pressure as function of distance from the two sides of the break. The numbers 1 to 25 refer to the incident mode, and Figures 5 (left) and 5 (right) show the corresponding total dynamic bottom pressure on the left and right sides of the break, respectively. For the left side (Figure 5, left), each incident mode results oscillatory nonevanescent total pressure contribution. However, for the right side only the gravity and evanescent modes exist for the leading eight modes. While the gravity mode does not have impact on the bottom pressure, the amplitudes of the evanescent modes decay exponentially with distance. Therefore, the first eight incident modes do not contribute to the dynamic bottom pressure at the far right field. However, a single acoustic-gravity mode (first mode) appears when considering incident modes 9 to 23, and an additional one (second mode) appears when considering the 24th incident mode or more. As an example, the incident mode $\hat{\imath} = 9$ results in the appearance of the first acoustic-gravity mode on the right side. This mode propagates with same frequency as of the ninth incident mode, $\omega_9 = 10.33$ rad/s but has a wavelength $\lambda = 2.23$ km which is shorter than the wavelength of the incident mode, $\lambda_9 = 3.70$ km (see Table 2).

[29] From Figure 5 we further conclude that for the left side of the break the lower incident modes dominate the flow at all x, whereas for the right side the lower modes dominate at the vicinity of the break at $x = 0^+$ while the higher modes dominate at $x > 0$ far from the break. The bottom subplots represent the superposed solution of all 25 incident modes, on the two sides of the break.

[30] Figure 6 presents temporal evolution of the dynamic bottom pressure at $|x| = 1$ km (Figure 6, top), $|x| = 10$ km (Figure 6, middle), and $|x| = 100$ km (Figure 6, bottom), for the problem with $N = 25$ incident modes. Compared to the case with $x = 0$ in Figure 3 the dynamic bottom pressure on the left side of the break remains of the same order of magnitude. On the other hand, the pressure on the right side of the break drops by 72% at $x = 1$ km, whereas no additional drop is noticed at $x = 10$ or $x = 100$ km.

[31] The pressure amplitude as function of the specific frequency of the incident (black bars) and transmitted (gray bars) acoustic-gravity modes is presented in Figure 7. The calculations are for $t = 2705$ s. The general trend is that the pressure amplitude decreases with the frequency, as observed

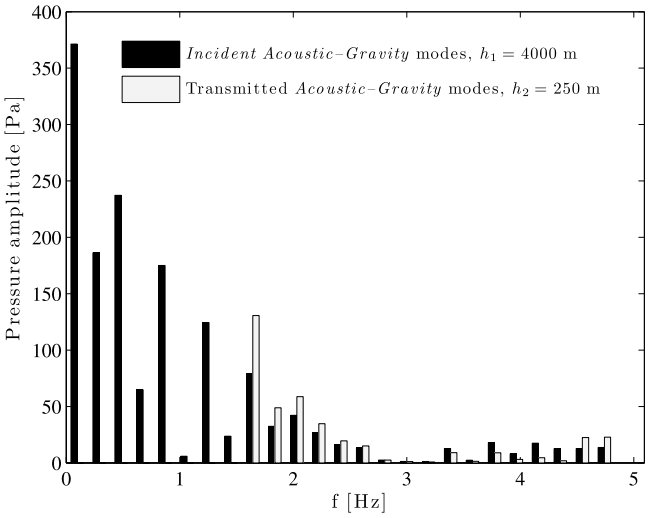

Figure 7. Pressure amplitude of the incident (black bars) and transmitted (gray bars) acoustic-gravity modes (at $t = 2705$ s).

in Figure 2, and that the low-frequency modes (<1 Hz) are dominating at $h_1 = 4000$ m. However, in the case of the transmitted modes, the frequency modes (>1.5 Hz) become dominant, as the low-frequency modes do not exist at $h_2 = 250$ m.

6. Concluding Remarks

[32] The two-dimensional problem of an acoustic-gravity wave mode propagating toward a bottom with a step in an inviscid and slightly compressible fluid has been addressed. The existence of acoustic-gravity modes depends on the water depth, h, and the frequency of propagation ω. The condition for existence implies that $\omega h > \pi C_s/2$.

[33] As an incident acoustic-gravity mode reaches a step, part of the energy is transmitted and the rest is reflected. The two parts are distributed among the allowed wave modes. The dynamic bottom pressure is calculated from the potential amplitudes of the transmitted and reflected modes.

[34] An example of acoustic-gravity waves, from a submarine earthquake, propagating toward a continental shelf has been examined in details.

6.1. At the Vicinity of the Shelf Break

[35] Calculations of the total dynamic bottom pressure at the vicinity of the break ($x = 0$) show that the magnitudes of the bottom pressure on both sides of the shelf break are of the same order.

[36] Values of the dynamic bottom pressure change with the number of evanescent modes. However, convergence is relatively fast. In the given example the difference in the bottom pressure when considering 30 additional evanescent modes is as low as 0.14% and 2.22% for the left and right sides of the break, respectively.

6.2. Away From the Shelf Break

[37] On the left side of the shelf break the lower incident modes dominate the flow both near and far from the break. There are always acoustic-gravity wave modes reflected for each incident mode. Therefore the dynamic bottom pressure has an oscillatory nonvanishing behavior. Since the leading acoustic-gravity modes all exist, the contribution of the evanescent modes to the bottom pressure is minor, and thus the decrease in pressure away from the break as the evanescent modes vanish is negligible.

[38] On the right side of the shelf break, transition occurs to much shallower water, where only high-frequency acoustic-gravity wave modes may prevail. In this case, the contribution of the evanescent modes to the dynamic bottom pressure (which decreases exponentially with distance) is significant. At a few kilometers from the break the contribution of the evanescent modes to the bottom pressure becomes small, and the bottom pressure is dominated by the acoustic-gravity modes with relatively high frequencies (>1 Hz). The bottom pressure drops by about 70% far from the break, that is, by the contribution of the evanescent modes.

[39] To summarize, while the contribution of evanescent modes is negligible anywhere in the deep ocean, it is significantly larger on the continental shelf, in particular at the vicinity of the shelf break.

6.3. Early Detection of Tsunami

[40] It is noticeable that the choice of $h_1 = 4000$ m is appropriate both for the 2004 Boxing Day tsunami and the 1960 Chile tsunami [e.g., *Constantin and Johnson*, 2008]. In both occurrences the gravity wave propagated with a velocity of about 200 m/s [e.g., *Segur*, 2008], which is considerably smaller than the velocity of the acoustic-gravity waves. Moreover, based on the bed friction given by *Nelson* [1995], which takes into account the bed particle size, total roughness due to sand grains, and Shields entrainment parameter, the damping of acoustic-gravity waves that travel a distance of 10^6 m turns out to be negligible. In that context, acoustic-gravity waves may travel few thousands of kilometers before dissipating, which is in agreement with *Bolshakova et al.* [2011], at least for the range of frequencies (>2 Hz), since the low-frequency modes can only be measured in the deep ocean where they exist. For that objective, there is a need for low-frequency hydrophones (currently under development), along with bottom seismometers and bottom pressure sensors, which could detect acoustic-gravity waves generated up to hundreds of kilometers from the epicenter (*Chierici et al.* [2010]). Therefore, the capability to measure the acoustic-gravity modes should be considered for early detection of tsunami as proposed, among others, by *Chierici et al.* [2010] and *Stiassnie* [2010].

[41] The dynamic bottom pressure could be sufficiently large for measurement purposes. However, determining the optimal location of measurement sensors could be fairly complicated. A prospective location is in the deep ocean at the vicinity of the shelf break, where the dynamic bottom pressure contains contributions both from incident and reflected wave modes, simultaneously.

[42] **Acknowledgment.** This research was supported by the Israel Science Foundation (grant 63/09).

References

Bolshakova, A., S. Inoue, S. Kolesov, H. Matsumoto, M. Nosov, and T. Ohmachi (2011), Hydroacoustic effects in the 2003 Tokachi-oki tsunami source, *Russ. J. Earth Sci.*, *12*, ES2005, doi:10.2205/2011ES000509.

Chierici, F., L. Pignagnoli, and E. Davide (2010), Modeling of the hydro-acoustic signal and tsunami wave generated by seafloor motion including

a porous seabed, *J. Geophys. Res.*, *115*, C03015, doi:10.1029/2009JC005522.

Constantin, A., and R. S. Johnson (2008), Propagation of very long water waves, with vorticity, over variable depth, with applications to tsunamis, *Fluid Dyn. Res.*, *40*, 175–211, doi:10.1016/j.fluiddyn.2007.06.004.

Kajiura, K. (1970), Tsunami source, energy and directivity of wave radiation, *Bull. Earthquake Res. Inst. Univ. Tokyo*, *48*(5), 835–869.

Miyoshi, H. (1954), Generation of the tsunami in compressible water (Part I), *J. Oceanogr. Soc. Jpn.*, *10*, 1–9.

Nelson, R. C. (1995), Wave bed friction damping over shoaling, movable beds, *Coastal Eng.*, *25*, 65–80.

Nosov, M. A. (1999), Tsunami generation in compressible ocean, *Phys. Chem. Earth, Part B*, *5*, 437–441, doi:10.1016/S1464-1909(99)00025-8.

Nosov, M. A., and S. V. Kolesov (2007), Elastic oscillations of water column in the 2003 Tokachi-oki tsunami source: In-situ measurements and 3-D numerical modelling, *Nat. Hazards Earth Syst. Sci.*, *7*, 243–249, doi:10.5194/nhess-7-243-2007.

O'Hare, T. J., and A. G. Davies (1992), A new model for surface wave propagation over undulating topography, *Coastal Eng.*, *18*, 251–266.

Segur, H. (2008), Integrable models of waves in shallow water, in *Probability, Geometry and Integrable Systems*, *Math. Sci. Res. Inst. Publ. Ser.*, vol. 55, edited by M. Pinsky and B. Birnir, pp. 345–371, Cambridge Univ. Press, Cambridge, U. K.

Sells, C. C. L. (1965), The effect of a sudden change in shape of the bottom of a slightly compressible ocean, *Philos. Trans. R. Soc. London, Ser. A 258*, 495–528.

Stiassnie, M. (2010), Tsunamis and acoustic-gravity waves from underwater earthquakes, *J. Eng. Math.*, *67*, 23–32, doi:10.1007/s10665-009-9323-x.

Yamamoto, T. (1982), Gravity waves and acoustic waves generated by submarine earthquakes, *Soil Dyn. Earthquake Eng.*, *1*, 75–82.

U. Kadri and M. Stiassnie, Faculty of Civil and Environmental Engineering, Technion Israel Institute of Technology, Haifa 32000, Israel. (usama.kadri@gmail.com)